Int J Adv Manuf Technol (2016) 84:2257–2264
DOI 10.1007/s00170-015-7852-1

ORIGINAL ARTICLE

Study on chip failure mechanism in high-speed cutting process with electronic theory

Jin-quan Li[1] · Rui Zhang[1] · Hai-lin Guo[1] · Zhi-jun Zhang[1]

Received: 26 March 2015 / Accepted: 13 September 2015 / Published online: 26 September 2015

Abstract In this paper, the microscopic mechanism of 080A15 and 30CrMnMo steel chip failure modes has been studied at the level of valence electron structure (VES) based on the empirical electron theory (EET) of solids and molecules. Studies show the bonding ability and the lattice electron density are related to the chip failure form. If the bonding ability is weak and the lattice electron density is high, the chip is more prone to ductile fracture. Conversely, the chip is more prone to adiabatic shear failure to form the serrated chip divided uniformly by adiabatic shear bands (ASBs). For 080A15 steel, the bonding force between atoms is weak, and the lattice electron density is very high. It is difficult to produce the thermal-mechanical instability. Thus, the chip was formed by ductile fracture. For 30CrMnMo steel, the total bonding ability of each structural unit of carbon and alloy elements is stronger, and the lattice electron density of each structural unit is weaker, the temperature can rise instantaneously to a very high level to form the serrated chip with the adiabatic shear failure. The results of this research provide useful insights on material design and selection in high-speed cutting by studying the specific alloy elements on the influence of chip failure mechanism at the VES level.

Keywords Electron structure · High-speed cutting · Adiabatic shear band · Serrated chip

1 Introduction

At present, the high-speed cutting technology has become the development direction of machining technology [1, 2]. During high-speed cutting process, the impact between the tool and workpiece confines shear deformation in a small area causing the temperature to rise up sharply to produce a thermal softening phenomenon to form the adiabatic shear band (ASB). At this extreme working condition, traditional cutting theory faces challenges to provide clear understanding of chip failure mechanism and influencing factors because of the high speed and difficulty of online detection [3].

Existing researches have shown that serrated chips with uniform interval of ASBs can occur in many materials in the process of high-speed cutting, high-speed grinding, high-speed milling, etc. These materials include hardened steel, Ni–Fe super alloy, nickel-based alloy, titanium alloy, and so on [4–13]. The serrated chip will affect the surface quality and tool wear and cause a high-frequency change of cutting force [14]. Therefore, the study of serrated chip failure mechanism is of great significance.

ASB is a localized deformation band produced under the condition of high strain rate, large strain, and heat concentration resulting from thermal-mechanical instability in a material when thermal softening exceeds strain hardening. It is usually the forerunner of material fracture [15]. There are two kinds of ASBs: one is phase-transformed ASB which is associated with microstructural changes and the other is deformed ASB composing of seriously distorted grains, flow lines, and large plastic deformation

Electronic supplementary material The online version of this article (doi:10.1007/s00170-015-7852-1) contains supplementary material, which is available to authorized users.

✉ Jin-quan Li
li_jinquan@163.com

[1] School of Mechanical Engineering, Shenyang Ligong University, No.6 Nanping Center Road, Hunnan New District, Shenyang 110159, China

without any phase change. The studies have shown that it is possible to produce a variety of microstructural changes in ASBs, such as phase transformation, dislocation, recrystallization, amorphization, and so on [16, 17].

The factors affecting the localized deformation of adiabatic shear are the intrinsic constitutive relation, thermophysical properties of materials, such as strength, thermal conductivity, density, and specific heat [18, 19], and external factors, such as cutting speed, cutting thickness, cutting tool rake angle, and so on. Among these factors, material property plays a very important role. The stronger the material strength or the smaller the thermal conductivity, the easier the occurrence of ASB as well [20, 21].

The difference of the density or specific heat is smaller for common steel materials. But the difference of the thermal conductivity or strength much affected by compositions and microstructures usually is very big. Thus, the main factors affecting the adiabatic shear failure are the thermal conductivity and strength under the same experimental condition—identical cutting speed, cutting thickness, and cutting tool rake angle.

At present, many studies on the failure mechanism of serrated chip have focused mostly on the tests and the effect of microstructure and properties of the materials based on macroscopic understanding; explanations are phenomenological. The studies are hard to break through in theory.

Due to material macro performance mainly relying on its microelectronic structure, it is of great significance to study the characteristics of serrated chip damage from the perspective of valence electron structure (VES) to design and select appropriate material based on the adiabatic shearing phenomena.

The empirical electron theory (EET) [22] based on Panling metal electronic theory was proposed by Professor Yu Ruihuang. It describes VES according to the atom hybrid state. The VES parameters of 78 elements have already been calculated in the EET, which are listed in the hybridization tables [23]. The material performance can be studied further from atom structure to the electron structure by the EET. Researchers have been studying the practical application of the EET for over 30 years. The research results about EET can be found in detail in [22–28]. The VES of inter-metallic compound and cast iron were analyzed [29–31], the calculation of the lattice constant of solids and the yield strength in some steels [32–34] were given, and the theoretical basis for the chemical composition design of titanium alloys was provided [35] using the VES parameters. The researchers have also studied the relationship between the VES and physical performance of material (melting point, boiling point, magnetism, and so on) [36–40].

Precisely because of these practical applications of the EET, it establishes the foundation for studying the micro failure mechanism of chip in the process of high-speed cutting from the level of the VES with the EET.

Therefore, in this paper, the micro failure mechanism of chip in the process of high-speed cutting was studied from the level of the VES with the EET.

Table 1 The chemical compositions of 080A15 steel (wt%)

C	Si	Mn	Cr	Ni
0.18–0.28	≤0.30	0.40–0.70	≤0.30	≤0.30

Table 2 The chemical compositions of 30CrMnMo steel (wt%)

C	Si	Mn	Cr	Mo
0.26–0.32	0.20–0.33	0.85–1.00	0.90–1.05	0.35–0.45

2 Experimental procedures

Two workpiece materials of 080A15 and 30CrMnMo steel pipes are used in this study. The diameter is 20 mm and the wall thickness is 1.5 mm. The manufacturing processes of the two steels are, respectively, converter smelting, refining, and rolling. The cutting test were carried out on the high-speed precision sawing machine using high-speed steel (HSS) saw blade whose type is $\phi 200 \times 3.0 \times 60Z$; the cutting speeds are ranged from 3100 to 13,800 m/min. The lengthwise streaking travel rate of the machine table is 180 m/min, max lateral travel is 2500 mm, and lengthwise position location accuracy is 0.1 mm. Metallographic specimens were made of chips for microscopic observation. The chemical compositions are shown in Tables 1 and 2. The thermal physical parameters are shown in Table 3 [41, 42].

3 Experimental results and discussion

3.1 The chip microscopic failure characteristics of 080A15 and 30CrMnMo steels

The original microstructure of the 080A15 steel workpieces is shown in Fig. 1. The different microstructure on the surface of the 080A15 steel chip at different cutting speeds is shown in

Table 3 The thermal physical parameters of the experimental steels

Materials	Tensile strength MPa	Thermal conductivity $W(m\ K)^{-1}$	Specific heat $J(kg\ K)^{-1}$	Density $kg\ m^{-3}$
080A15A	450	65	745	7.8×10^3
30CrMnMo	1100	31.90	587	7.8×10^3

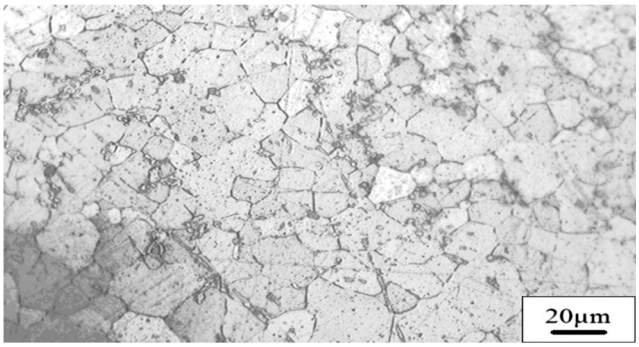

Fig. 1 The original microstructure of the 080A15 steel workpiece

Fig. 2. There are many stripes on the surface of the chip under the speed of 5000 m/min, as shown in Fig. 2a; grain deformation is severe at the speed of 7500 m/min, as shown in Fig. 2b; there are many grooves showing good plastic liquidity on the surface of the chip at the speed of 11,300 m/min, as shown in Fig. 2c; and the recrystallization makes grains dense and fine at the speed of 13,800 m/min, as shown in Fig. 2d, but there is no ASB at all.

For 30CrMnMo steel, the area in Fig. 3a where the white arrows are pointing to is the original microstructure. ASBs were found by scanning electron microscope and metallographic microscope in the chip. The deformed ASBs in which the grain deformation was severe but the structure did not change occurred at the speed of 5000 m/min, as shown in the white square of Fig. 3a where the white arrows are pointing, and the phase-transformed ASBs, on both sides of which the grain deformation was severe, were found at the speed of 7500 m/min, as shown in the black stripe of Fig. 3b. The serrated chips divided uniformly by ASBs were produced, as shown in Fig. 3c, d.

3.2 The VES calculation of 080A15 and 30CrMnMo steels

080A15 steel is supersaturated interstitial solid solution that C is in α–Fe. The Fe–C crystal cell in 080A15 steel is shown in Fig. 4.

Fe1, Fe2, and Fe3 are, respectively, Fe atom of different positions, and the C atom is in the center of the Fe–C crystal cell. The lattice constants of the Fe–C crystal cell can be calculated with the carbon content (C wt%=0.2) [23]. That is a_c=0.26784 and c_c=0.37876 nm.

Between μ and ν atoms, all the experiment bond length $D_{n\alpha}^{\mu\nu}$ (unit: nm) of the Fe–C crystal cell in 080A15 steel can be calculated by the lattice constant (a_c and c_c) and the geometrical structure (Fig. 4). They are as the following:

$$D_{nA}^{\text{C-Fe1}} = \frac{1}{2}c_c = 0.18938 \tag{1}$$

$$D_{nB}^{\text{C-Fe2}} = \frac{\sqrt{2}}{2}a_c = 0.18939 \tag{2}$$

$$D_{nC}^{\text{Fe1-Fe2}} = \left[\left(\frac{\sqrt{2}}{2}a_c\right)^2 + \left(\frac{1}{2}c_c\right)^2\right]^{\frac{1}{2}} = 0.26783 \tag{3}$$

$$D_{nD}^{\text{Fe2-Fe3}} = \left[\left(\frac{\sqrt{2}}{2}a_c\right)^2 + \left(\frac{1}{2}c_c\right)^2\right]^{\frac{1}{2}} = 0.26783 \tag{4}$$

$$D_{nE}^{\text{Fe2-Fe2}} = a_c = 0.26784 \tag{5}$$

$$D_{nF}^{\text{C-Fe3}} = \left[a_c^2 + \left(\frac{1}{2}c_c\right)^2\right]^{\frac{1}{2}} = 0.32803 \tag{6}$$

$$D_{nG}^{\text{Fe3-Fe3}} = c_c = 0.37876 \tag{7}$$

$$D_{nH}^{\text{Fe3-Fe3}} = \sqrt{2}a_c = 0.37878 \tag{8}$$

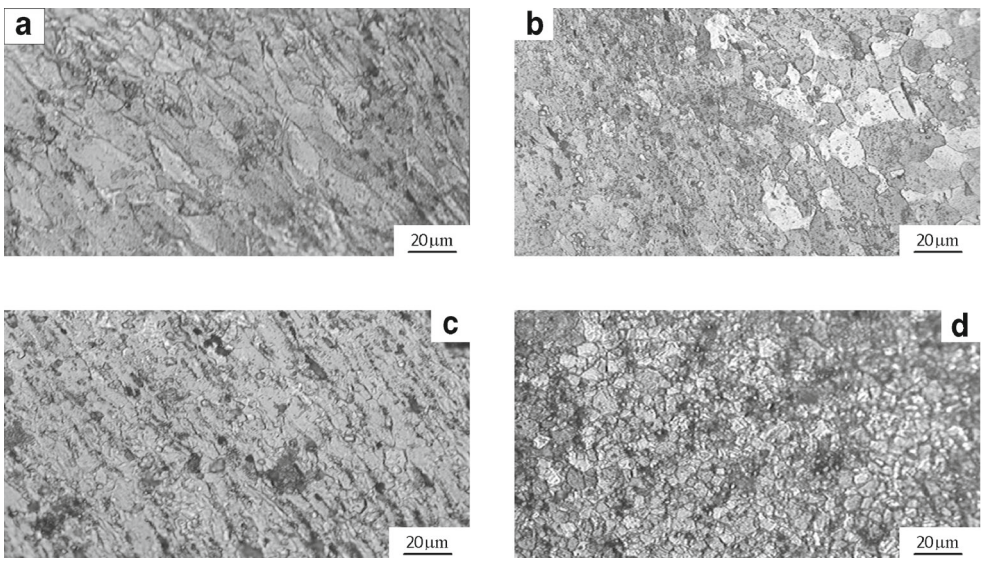

Fig. 2 The different microstructure in the 080A15 steel chips: **a** v=5000 m/min, **b** v=7500 m/min, **c** v=11,300 m/min, **d** v=13,800 m/min

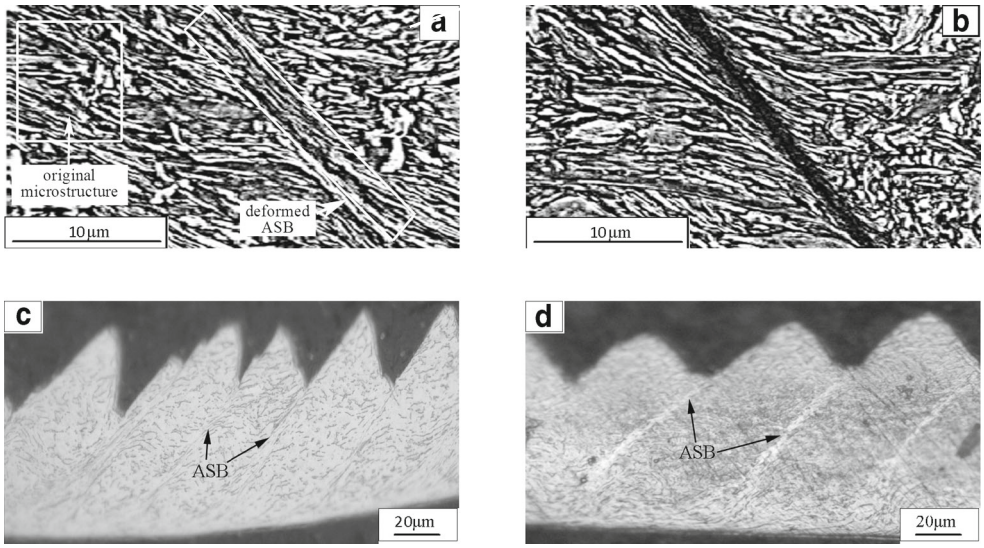

Fig. 3 The ASB microstructure in the 30CrMnMo steel chips: **a** v=5000 m/min, **b** v=7500 m/min, **c** the serrated chip with deformed ASB, **d** the serrated chip with transformed ASB

The covalent bond length calculated by the covalent electron pair number n_α is called theoretical bond length $\overline{D}_{n\alpha}^{\mu v}$. n_α is covalent electron pair number of α bond (α=A, B, C, ……, N represent all covalent bonds in a structural unit, $n_A$is the biggest one.)

Each atom is generally formed by the hybridization of the h and t states in the EET. The two kinds of states have respectively its own single bond radii $R(I)$, dumb pair electrons n_d, magnetic electron n_m, lattice electron n_l, covalent electron n_c, and total valence electron n_T. The different material properties are determined by these VES parameters. The hybridization of h and t states has many possibilities called the number of hybrid level. There are different theoretical bond lengths with different VES parameters in every hybrid level σ.

The theoretical bond length $\overline{D}_{n\alpha}^{\mu v}$ corresponds with the experimental one $D_{n\alpha}^{\mu v}$ if the difference between $\overline{D}_{n\alpha}^{\mu v}$ and $D_{n\alpha}^{\mu v}$ is $\Delta D = \left|\overline{D}_{n\alpha} - D_{n\alpha}\right| \le 0.005$ nm, namely the VES parameters at this hybrid level σ corresponds with the actual atom status. Therefore, we can determine the covalence bond net and the hybrid level of all kinds of atoms. It means that the VES is also determined. This is called bond length difference (BLD) method. The VES of 080A15 were obtained using the BLD method [43], as shown in Table 4.

The lattice electron density is defined as the ratio of the total of lattice electron number and the total of valence electron number in a cell. For the Fe–C cell, the lattice electron density is

$$\rho_{\text{Fe-C}} = \frac{\sum n_l}{\sum n_T} = \frac{n_{l12}^{Fe1} + 2n_{l10}^{Fe2} + n_{l9}^{Fe3} + n_{l6}^{C}}{n_{T12}^{Fe1} + 2n_{T10}^{Fe2} + n_{T9}^{Fe3} + n_{T6}^{C}} \times 100\% = 24.54\% \quad (9)$$

There are Fe–C–Me and Fe–C–Me^x–Me^y structural units in the 30CrMnMo steel. Where Me is alloying element. The VES of Fe–C–Me structural units can be calculated with the same method.

Limited by space, only the lattice electron density and the VES parameters related to the bonding ability (Eq. 13) for the structural units containing carbon and alloy elements are shown in Table 5.

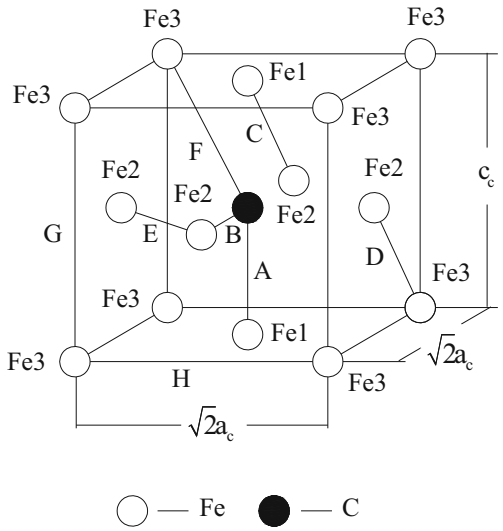

Fig. 4 The crystal cell of Fe–C

3.3 The calculation of total bonding ability of structural units containing C atoms in 080A15 and 30CrMnMo steels

The bonding ability F_α of α band formed by u and υ atoms is arithmetic mean of their respective bonding ability f in the EET [27, 28].

$$F_\alpha = \frac{1}{2}(f_u + f_\upsilon) \quad (10)$$

Table 4 The VES parameters of Fe–C cell in 080A15 (C wt%=0.2)

Fe–C cell $\rho_{\text{Fe-C}}$=24.54%	Fe1 σ=A12 n_{l12}^{Fe1}=1.0422 $n_{\text{T12}}^{\text{Fe1}}$=5.4025	Fe2 σ=A10 n_{l10}^{Fe2}=1.3518 $n_{\text{T10}}^{\text{Fe2}}$=5.3241	Fe3 σ=A9 n_{l9}^{Fe3}=1.4838 $n_{\text{T9}}^{\text{Fe3}}$=5.2591	C σ=6 n_{l6}^{C}=0 n_{T6}^{C}=4
Bond name	$D^{\mu\nu}_{n\alpha}$ (nm)	$\overline{D}^{\mu\nu}_{n\alpha}$ (nm)	n^{α}	$\Delta D^{n\alpha}$ (nm)
$D_{nA}^{\text{C-Fe1}}$	0.18938	0.18883	0.8060	0.00055
$D_{nB}^{\text{C-Fe2}}$	0.18939	0.18882	0.7976	0.00057
$D_{nC}^{\text{Fe1-Fe2}}$	0.26783	0.26728	0.1839	0.00055
$D_{nD}^{\text{Fe2-Fe3}}$	0.26783	0.26728	0.2143	0.00055
$D_{nE}^{\text{Fe2-Fe2}}$	0.26784	0.26729	0.2046	0.00055
$D_{nF}^{\text{C-Fe3}}$	0.32803	0.32748	0.0105	0.00055
$D_{nG}^{\text{Fe3-Fe3}}$	0.37876	0.37821	0.0061	0.00055
$D_{nH}^{\text{Fe3-Fe3}}$	0.37878	0.37823	0.0059	0.00055

For the atom of *s-p-d* hybridization, there is

$$f = \sqrt{\alpha} + \sqrt{\alpha\beta} + g\sqrt{5\gamma}. \tag{11}$$

where α, β, and γ represents, respectively, the compositions of s, p, and d electrons in the hybrid orbital, and g is the contribution of electron spin orbit coupling effect to the bonding ability, for elements in the 4th, 5th, and 6th periods of the periodic Table, g=1, 1.35, and 1.70, respectively.

$$\left.\begin{aligned} \alpha &= (l\tau C_{h\sigma} + l'\tau' C_{t\sigma})/n_{T\sigma} \\ \beta &= (mC_{h\sigma} + m'C_{t\sigma})/n_{T\sigma} \\ \gamma &= (nC_{h\sigma} + n'C_{t\sigma})/n_{T\sigma} \end{aligned}\right\} \tag{12}$$

where l, m, n, and l',m',n' are, respectively, the number of covalent electrons and lattice electrons of s, p, d electrons in the h and t states. τ and τ' are, respectively, the parameters related to the h and t states, and value 0 when the s electron is lattice electron and value 1 when s electron is covalent electron. $C_{t\sigma}$ and $C_{h\sigma}$ is, respectively, the compositions of the t and h states at a certain hybrid level σ. $n_{T\sigma}$ is the total valence electron number at a certain hybrid level σ.

F is defined as the total bonding ability of all bands containing C atoms in a structural unit.

$$F = \sum n_\alpha F_\alpha \tag{13}$$

where n_α is the covalent electron pair number of the α bond containing C atom.

For 080A15 steel, the Table 4 shows that the hybrid level σ of C atom is 6, and the hybrid levels σ of Fe1, Fe2, and Fe3 atoms are, respectively, A12, A10, and A9 for Fe–C structure unit. Therefore, the parameters calculating the bonding ability are obtained from Tables 4 and 6 [23].

Thus, the total bonding ability of all bands containing C atoms in the Fe–C structural unit can be obtained by Eqs. 10–13. That is

$$\begin{aligned} F_{\text{Fe-C}} &= \sum n_\alpha F_\alpha = n_A F_{\text{C-Fe1}} + n_B F_{\text{C-Fe2}} + n_F F_{\text{C-Fe3}} \\ &= 3.7336 \end{aligned}$$

For 30CrMnMo steel, the C–Mo, C–Cr, and C–Mn bonds are added in 30CrMnMo steel contrasting with 080A15 steel. According to the hybrid levels σ of C, Fe, Cr, Mn, and Mo atoms (Table 5), the parameters calculating the bonding ability can be obtained from Table 6. Similarly, the total bonding ability of the Fe–C–Mo, Fe–C–Cr, and Fe–C–Mn structural units can be calculated, as shown in Table 7.

In order to facilitate the comparison, the total bonding ability F, the biggest covalent electron pair number n_A, and the lattice electron density ρ are listed in Table 7.

Table 5 The VES parameters of Fe–C–Me cell in 30CrMnMo (C wt%=0.3)

Fe–C–Cr, $\rho_{\text{C-Cr}}$=19.52%		Fe–C–Mn, $\rho_{\text{C-Mn}}$=17.52%		Fe–C–Mo, $\rho_{\text{C-Mo}}$=8.70%	
Cr: σ=6, Fe2: σ=A12, Fe3: σ=A9, C: σ=6		Mn: σ=A2, Fe2: σ=A12, Fe3: σ=A10, C: σ=6		Mo: σ=A1, Fe2: σ=A16, Fe3: σ=A15, C: σ=6	
Bond name	n_α	Bond name	n_α	Bond name	n_α
$D_{nA}^{\text{C-Cr}}$	1.1072	$D_{nA}^{\text{C-Mn}}$	1.1184	$D_{nA}^{\text{C-Mo}}$	2.6272
$D_{nB}^{\text{C-Fe2}}$	0.7605	$D_{nB}^{\text{C-Fe2}}$	0.7907	$D_{nB}^{\text{C-Fe2}}$	0.5261
$D_{nF}^{\text{C-Fe3}}$	0.0106	$D_{nF}^{\text{C-Fe3}}$	0.0098	$D_{nF}^{\text{C-Fe3}}$	0.0065

Table 6 The VES parameters for calculating the bonding ability

Structural unit	Atom	Hybrid level σ	l	m	n	τ	l'	m'	n'	τ'	$C_{h\sigma}$	$C_{t\sigma}$	$n_{T\sigma}$
Fe- C	Fe1	A12	2	1	2	0	1	1	4	1	0.5211	0.4789	5.4789
	Fe2	A10	2	1	2	0	1	1	4	1	0.6759	0.3241	5.3241
	Fe3	A9	2	1	2	0	1	1	4	1	0.7419	0.2591	5.2591
	C	6	2	2	0	0	1	3	0	1	0	1	4
Fe–C–Mo	Mo	A1	2	2	2	0	1	0	3	1	1	0	6
	Fe2	A16	2	1	2	0	1	1	4	1	0.0544	0.9456	5.9456
	Fe3	A15	2	1	2	0	1	1	4	1	0.1002	0.8998	5.8998
	C	6	2	2	0	0	1	3	0	1	0	1	4
Fe–C–Mn	Mn	A2	1	2	2	0	1	2	4	1	0.9945	0.0055	5.0111
	Fe2	A12	2	1	2	0	1	1	4	1	0.5211	0.4789	5.4789
	Fe3	A10	2	1	2	0	1	1	4	1	0.6759	0.3241	5.3241
	C	6	2	2	0	0	1	3	0	1	0	1	4
Fe–C–Cr	Cr	6	2	1	3	0	1	1	1	1	0.6807	0.3193	5.0421
	Fe2	A12	2	1	2	0	1	1	4	1	0.5211	0.4789	5.4789
	Fe3	A9	2	1	2	0	1	1	4	1	0.7419	0.2591	5.2591
	C	6	2	2	0	0	1	3	0	1	0	1	4

3.4 The chip failure microscopic mechanism of the 080A15 and 30CrMnMo steels

The experimental results of the above two materials under the same experimental conditions are obviously different. The main difference between 080A15A and 30CrMnMo steels is that 30CrMnMo steel contains different alloy elements.

The phase transformation of alloys is the process of the old covalent bond rupture and the new covalent bond formation. The covalent bond formed between atoms in solids is the skeleton which constitutes the entire unit cell. Therefore, the stronger the total bounding ability of unit cell is, the more difficult the rupture of covalent bond, the more powerful the phase transformation resistance, and the higher the strength and hardness is.

The calculation results of VES show that the total bonding capability of Fe–C structure unit in the 080A15 steel is $F_{\text{Fe-C}}$= 3.7336, and the total bonding capabilities of Fe–C–Mo, Fe–C–Mn, and Fe–C–Cr units in the 30CrMnMo steel are $F_{\text{Fe-C-Mo}}$=7.4859, $F_{\text{Fe-C-Mn}}$=4.4130 and $F_{\text{Fe-C-Cr}}$=4.3026, respectively. Each bonding ability of these units containing alloy elements is stronger than that of Fe–C structural unit in the 080A15.

Therefore, the phase transformation is difficult in the structural units containing alloy elements, so that the resistance to dislocation motion and the stability and the strength of the alloy steel are all increased. Just as mentioned above, the tensile strength of 080A15 and 30CrMnMo steels is 450 and 1100 MPa, respectively (Table 3).

The lattice electron can be free to move in the interstitial void, and the lattice electron's directional migration forms the electric current under an external field in the EET [23]. Consequently, the higher the lattice electron density, the higher the electrical conductivity. The metal thermal conductivity is proportional to the electrical conductivity according to Wiedemann-Franz-Lorentz law. Thus, the decrease of the lattice electron density means a decrease of crystal thermal conductivity.

The lattice electron density of structure unit Fe–C in 080A15 steel is highest (24.54 %) compared to Fe–C–Mo, Fe–C–Cr, and Fe–C–Mn. The lattice electron density of structure units Fe–C–Mo, Fe–C–Cr, and Fe–C–Mn is, respectively, 8.70, 9.52, and 17.52 % in 30CrMnMo steel (Table 7). This demonstrates that the lattice electron density is reduced after adding the alloy elements Cr, Mn, and Mo, namely the thermal conductivity is reduced. In particular, the sharp decline in the thermal conductivity is due to the huge drop of the lattice electron density after adding the alloy element Mo. The thermal conductivity of 080A15 and 30CrMnMo steels is 65 and 31.9 $W(m\ K)^{-1}$, respectively (Table 3).

In summary, the failure mode of chip relates to the total bonding capability of structure units and the lattice electron

Table 7 The VES of Fe–C–Me and Fe–C

Structure unit	F	n_A	ρ (%)
Fe–C–Mo	7.4859	2.6272	8.70
Fe–C–Cr	4.3026	1.1072	9.52
Fe–C–Mn	4.4130	1.1184	17.52
Fe–C	3.7336	0.8060	24.54

density from the perspective of VES. The stronger the total bonding capability is, the higher the strength and the easier the formation of serrated chip with ASBs is. Also, the lower the lattice electron density is, the lower the thermal conductivity and the easier the formation of serrated chip with ASBs is. Therefore, it can be predicted to a certain extent by calculating the value F of the total bonding capability and the lattice electron density ρ whether the serrated chip is produced or how the serration segmented degree shows. So to some extent, this study about the influence law of specific alloy elements on the chip failure microscopic mechanism provides a new theoretical basis to design and select appropriate cutting material to improve the workpiece surface quality by the calculation of VES from the level of electronic structure.

4 Conclusions

- The factors influencing the chip failure mechanism are the total bonding capability and the lattice electron density from the perspective of VES. Chip failure mechanism is a function of the parameters of the total bonding capability and the lattice electron density.
- The stronger the total bonding capability or the lower the lattice electron density, the easier the formation of serrated chip with ASBs. To a certain extent, the formation of serrated chip can be predicted by calculating the VES parameters with the method of BLD in EET.
- To some extent, this study about the influence law of specific alloy elements on the chip failure microscopic mechanism provides a new theoretical basis to design and select appropriate cutting material to improve the workpiece surface quality by the calculation of VES from the level of electronic structure.

Acknowledgments This work is financially supported by the National Natural Science Foundation of China (Grant No.51275317/E050901 and 51175063/E050901).

References

1. Abukhshim NA, Mativenga PT, Sheikh MA (2006) Heat generation and temperature prediction in metal cutting: a review and implications for high speed machining. Int J Mach Tools Manuf 46(7–8):782–800
2. Ye GG, Xue SF, Ma W, Jiang MQ, Ling Z, Tong XH, Dai LH (2012) Cutting AISI 1045 steel at very high speeds. Int J Mach Tools Manuf 56:1–9
3. Liu ZQ, Zhang KG (2011) Sensitivity analysis of Johnson-Cook material constants on adiabatic shear. Chin J Aeronaut 32:2140–2146
4. Schulz H, Abele E, Sahm A (2001) Material aspects of chip formation in HSC machining. CIRP 50(1):45–48
5. Shih AJ, Luo J (2004) Chip morphology and forces in end milling of elastomers. J Manuf Sci Eng ASME 126:124–130
6. Ohbuchi Y, Obikawa T (2002) Evaluation of grindability of materials based on abrasive cutting simulation. Trans Jpn Soc Mech Eng 68:315–322
7. Yang QB, Liu ZQ, Wang B (2012) Characterization of chip formation during machining 1045 steel. Int J Adv Manuf Technol 63:881–886
8. Yang QB, Liu ZQ, Shi ZY, Wang B (2014) Analytical modeling of adiabatic shear band spacing for serrated chip in high-speed machining. Int J Adv Manuf Technol 71:1901–1908
9. Barry J, Byrne G (2002) The mechanisms of chip formation machining hardened steels. J Manuf Sci Eng ASME 124:528–535
10. Wang CY, Xie YX, Zheng LJ, Qin Z, Tang DW, Song YX (2014) Research on the chip formation mechanism during the high-speed milling of hardened steel. Int J Mach Tools Manuf 79:31–48
11. Dong G, Zhaopeng H, Rongdi H, Yanli C, Muguthu JN (2011) Study of cutting deformation in machining nickel-based alloy inconel718. Int J Mach Tools Manuf 51:520–527
12. Wang H, To S, Chan CY, Cheung CF, Lee WB (2011) Dynamic modelling of shear band formation and tool-tip vibration in ultra-precision diamond turning. Int J Mach Tools Manuf 51:512–519
13. Gu LY, Wang MJ (2013) Experimental and theoretical research on critical characteristics for adiabatic shear localization fracture in high-speed machining. Int J Adv Manuf Technol 68:1231–1240
14. Khrais SK, Lin YJ (2007) Wear mechanisms and tool performance of TiAlN PVD coated inserts during machining of AISI 4140 steel. Wear 262:64–69
15. Xu YB, Bai YL (2007) Shear localization, microstructure evolution and fracture under high-strain rate. Adv Mech 37:498
16. Xu YB, Zhang J, Bai YL, Meyers M (2008) Shear localization in dynamic deformation: microstructural evolution. Metall Mater Trans A 39A:811
17. Duan CZ, Wang MJ (2013) A review of microstructural evolution in the adiabatic shear bands induced by high speed machining. Acta Metall Sin 26:97–112
18. Dodd B, Bai YL (1992) Adiabatic shear localization. Pergamon Press, New York
19. Wright TW (2002) The physics and mathematics of adiabatic shear bands. Cambridge University Press, Cambridge
20. Bäker M, Rösler J, Siemers C (2003) The influence of thermal conductivity on segmented chip formation. Comput Mater Sci 26:175–182
21. Poulachon G, Moisan AL (1999) Hard turning: chip formation mechanisms and metallurgical aspects. J Manuf Sci Eng 122:406–412
22. Yü RH (1978) The empirical electron theory of solids and molecules. Chin Sci Bull 4:217–224
23. Zhang RL (1992) The empirical electron theory of solids and molecules. Jinlin Science and Technology Publishing House, Changchun
24. Liu ZL, Li ZL, Sun ZG (1999) Catalysis mechanism and catalyst design of diamond growth. Metall Mater Trans A 30A:1999–2757
25. Li ZL, Xu HB, Gong SK (2004) Texture formation mechanism of vapor-deposited fcc thin film on polycrystal or amorphous substrate. J Phys Chem B 108:15165–15171
26. Guo YQ, Yü RH, Zhang RL, Zhang XH, Tao K (1998) Calculation of magnetic properties and analysis of valence electronic structures of $LaT_{13-x}Al_x$ (T=Fe, Co) compounds. J Phys Chem B 102(1):9–16
27. Liu ZL, Li ZL, Liu WD (2002) Interface electron structure and interfacial properties. Science Publishing House, Beijing
28. Liu ZL (1990) Valence electron structure and composition design of alloy. Jinlin Science and Technology Publishing House, Changchun
29. Peng K, Yi M, Ran L, Ge Y (2011) Effect of the W addition content on valence electron structure and properties of $MoSi_2$-based solid solution alloys. Mater Chem Phys 129(3):990–994

30. Liu ZL, Li ZL, Sun ZG, Yang XP, Chen M (1995) Valence electron structure of cast iron and graphitization behavior criterion of elements. Sci China Ser A Math 38(12):1484–1491
31. Mi G, Li P, He L, Попель ПС (2010) EET research on melt structural information of magnesium alloy. Rare Met Mater Eng 39: 1881–1887
32. Liu ZL, Liu WD, Lin C (2004) Prediction of end-roll strength and rapid adjustment of the on-the-spot composition in automobile cross-beam steel. Prog Nat Sci 14(12):1104–1108
33. Liu ZL, Lin C, Liu Y, Guo Y (2005) Calculation of the yield and tensile strength in the alloying non quenched-tempered steel by the electron structure parameters. Prog Nat Sci 15:832–837
34. Liu WS, Feng PZ, Wang XH, Niu JA, Shen CJ, Liu JT (2012) Calculation and analysis of the valence electron structure of $MoSi_2$ and $(Mo_{0.95}, Nb_{0.05})Si_2$. Mater Chem Phys 132(2–3):515–519
35. Lin C, Yin GL, Zhao YQ, Ge P, Liu ZL (2011) Analysis of the effect of alloy elements on martensitic transformation in titanium alloy with the use of valence electron structure parameters. Mater Chem Phys 125(3):411–417
36. Yü RH (1982) Analysis of valence electron and magnetic moment structures of α-Fe, γ-Fe and Fe_4N—electron theory of case hardening α-toγ-Fe phase transformation and certain other related processes. Acta Metall Sin 18:337–347
37. Liu Z-L, Niu H-J, Jin C-F, Wang B (1989) A theory of C-Si segregation in Fe-C-Si alloys (I). Chin Sci Bull 34:100–104
38. Liu ZL, Lin C, Guo Y (2006) Theoretical calculation of the finishing rolling elongation in alloying non-quenched and tempered steel. Prog Nat Sci 16:859–867
39. Yü RH (1984) Interpretation of melting point and certain other physical and chemical properties of CrO_3, δ-CrO_2, Cr_2O_3, α-Al_2O_3 by their valence electron structures. J Struct Chem 03:193–208
40. Lin C, Zhao Y, Yin G (2015) Calculation of the lattice constant of solids with the use of valence electron structure parameters. Comput Mater Sci 97(1):86–93
41. Liu H-j, Cao J-g, Wang B-f, Li J-c, Xu Z-h (2010) 30CrMnMo numerical simulation of quenching seamless tube. J Inn Mong Univ Sci Technol 29(3):238
42. Lu JM (2004) The practical manual of mechanical engineering materials. Liaoning Science and Technology Publishing House, Shenyang
43. Li J-q, Huang D-w, Wang M-j (2010) Effect of valence electron structures of different targets on deformations of tungsten alloy penetrators. J Mater Eng 07:61